IEEE Access
Multidisciplinary | Rapid Review | Open Access Journal

Received 21 September 2022, accepted 9 October 2022, date of publication 13 October 2022, date of current version 19 October 2022.

Digital Object Identifier 10.1109/ACCESS.2022.3214232

APPLIED RESEARCH

Wind Turbine Micro-Doppler Prediction Using Unscented Kalman Filter

KAREL JURYCA[1], (Member, IEEE), JAN PIDANIC[1], (Senior Member, IEEE), AMIT K. MISHRA[2], (Senior Member, IEEE), ZLATAN MORIC[3], AND PAVEL SEDIVY[4], (Senior Member, IEEE)

[1]Department of Electrical Engineering, Faculty of Electrical Engineering and Informatics, University of Pardubice, 53210 Pardubice, Czech Republic
[2]Department of Electrical Engineering, University of Cape Town, Cape Town 7700, South Africa
[3]Cyber Security Department, Algebra University College, 10000 Zagreb, Croatia
[4]RETIA, a.s., 53002 Pardubice, Czech Republic

Corresponding author: Jan Pidanic (jan.pidanic@upce.cz)

This work was supported by the European Regional Development Fund (ERDF)/European Social Fund (ESF) "Cooperation in Applied Research Between the University of Pardubice and Companies in the Field of Positioning, Detection and Simulation Technology for Transport Systems (PosiTrans)" under Grant CZ.02.1.01/0.0/0.0/17_049/0008394.

ABSTRACT With the increasing focus on green energy, wind turbines (WTs) have become common occurrences in most landscapes. The presence of WTs in the field of view of a radar will create very complicated clutter in a received signal. One of the major reasons for the complicated nature of WT clutter is the fact that it will consist of a wide band of Doppler frequencies. In addition, the Doppler band of frequencies keep changing based on wind speed and direction The tracking of dominant Doppler frequencies is one of the most important steps in the process of filtering WT clutter. In this work, we present an unscented Kalman filter (UKF) based solution to track the dominant Doppler frequencies in WT echoes. We have shown the efficiency of our algorithm by applying it to a wide range of real-measured data collected from various locations in Europe.

INDEX TERMS Adaptive Kalman filtering, adaptive signal processing, Doppler effect, filter, radar.

I. INTRODUCTION

Many emerging applications require radar systems allowing detection of low, small, and slow (LSS) targets. LSS targets, however, often operate in environments with large structures that cause hard-on-model clutters. With the exponential increase in the building of wind farms, wind turbines (WTs) have proved to be one of the largest sources of such clutter [1], [2], [3], [4]. The usual location of a WT is on the coast, offshore, on the top of a hill, or mountain ridge. The most common WT type is a three blades WT, and hence this work will focus only on this type of WT.

The major influence of the WT on the radar system is the masking or exacerbating detection of the target detection (especially LSS targets) in the corresponding radar cell(s). However, WT influence can also cause other problems such as a false alarm, track seduction, limitation of the probability detection, etc. The masking effect affects not only the radar cell where a WT is placed, but also the neighbouring cells. The detailed information about WT's influence on the radar system is described in part II.

The general detection capabilities of the radar system can be limited by the (1) unwanted reflections from the natural environment, domestic or industrial buildings, etc. (generally static objects), and (2) unwanted echoes with strong micro-Doppler shifts caused by moving parts of objects. The first type of unwanted echoes obtained from static objects can be easily suppressed by standard suppression techniques [5], [6], [7], [8], [9].

For a radar system, the WT represents an obstacle that affects the received radar signal. The WT includes a static (tower, nacelle) and moving part (propeller blades). The echoes obtained from the obstacle effect can be divided into categories such as (1) back reflections, (2) mirror reflections,

The associate editor coordinating the review of this manuscript and approving it for publication was Prakasam Periasamy.

(3) wave diffraction, and (4) shadowing of objects behind the obstacle. Categories (2)-(4) usually do not pose a significant problem. Neglecting these echoes/reflections is allowed when dimensions of the propeller blades or tower of the WT are significantly smaller than the area covered by the main beam of the radar antenna. In this case, most of the transmitted energy passes around these obstacles. The major problem is thus represented by back reflections.

Current state-of-the-art mitigation techniques for active suppression of the effect of a WT on a radar system are very complex problem. Usually, they utilize various modifications of existing radar system hardware and/or advanced signal processing techniques. Known mitigation techniques are based on several approaches [10], [11], for example: (1) Cancelling resolution cell affected by WTs (SW approach) (2) Employing infill radars in or around the WT farm to maintain existing radar coverage (HW approach) (3) Fusing data from multiple sensors (HW) (4) Using special radiation absorbent material (RAM) paint for the WT (solution on the WT side) or absorbent materials (5) Utilizing advanced filtering techniques that enable mitigation of the interference from the WT (HW and SW approach).

Cancelling of the resolution cell affected by WTs is the simplest approach. It is not exactly a method of mitigation, but the radar system will ''ignore'' resolution cells where WTs are located. The information about targets in affected resolution cells is not available or can be distorted. This solution may be suitable for standalone WTs where the loss of information about the detected targets of interest is within one or a few radar resolution cells. For wind farms, this technique cannot be used as it would cancel a large part of the area of interest (e.g., wind farms on the UK coast [12]).

The second approach is based on employment of the infill radar and its placement to the area of a WT farm [13], [14], [15]. Industrial companies have developed several solutions for the infill radar. The TERMA company [16] developed a 2D coherent SCANTER 4002 radar, working on X-band, [17] with advanced MTI processing. Raytheon Technologies developed a mitigation wind farm solution that is adaptive for the specific environment and improves probability of detection of targets around the wind turbines based on NATS En-route radars. [18], [19]. The British company THRUPUT developed clutter processing equipment in the analogue domain (MIDAS III ACMS [20]), digital domain (RADIX DCMS [21]), and infill radar that cooperates with analogue and digital radars (RADIX IRI [22]). The infill radar solution is suitable only for a non-mobile radar system. The AVEILLANT company developed a 3D holographic radar THEIA 16A [23] working in L-band with coverage of $90° \times 90°$ and a range up to 10 km. The 3D holographic radar could mitigate clutter from WTs, vehicles, sea clutter, etc. Mobile infill radar C-SPEED [24] is produced by the Lightwave Radar company. It's a 2D surveillance radar working in S-band with a range up to 37 km. The main disadvantage is the high price of the solution and necessity of additional HW equipment that needs to cooperate with a radar system.

Overlapping sensor coverage and consequent fusion of information from an individual radar sensor increase the probability of the target detection/tracking in the area of the WT or wind farm location. From the WT side, it is possible to use a special material for blades that significantly reduces the level of radar signal reflection or Radar Cross Section (RCS) by electromagnetic wave absorption. [25], [26], [27], [28], [29].

The next approach is based on advanced filtering techniques that can be used as a hardware or software solution. The typical example of the hardware solution is a SMARTENER from the Cyrrus company [30] that uses data from an existing surveillance radar and determines from known WT positions whether the reflections are from the WT or the target of interest.

The universal software mitigation technique, until the present day, is not known (or not published). The difficulties of this universal technique approach are mainly through identification of WT signature and extremely high time-variability in the spectral domain.

The problem with wind turbine back reflections is that the individual parts of the wind turbine propeller blades move at a tangential velocity in the range from 0 to 220 m/s (791 km/h) from the centre of a WT to the end of the individual blade. Thus, the Doppler spectrum of these reflections generally covers the entire range of processed frequencies of reflections from targets of interest. The variation of the Doppler spectrum changes over time in a very complicated manner, and the intensity of these reflections greatly exceeds those of the targets of interest. The highest Doppler shifts will be at the end of the blade (edge), and this corresponds to the highest tangential speed of blades. The Doppler spectrum always contains three maxima that correspond to the Doppler shift of the ends of individual blades. The behaviour of the three dominant spectral components is also variable from the point of view of Doppler frequencies and amplitudes of the individual components. Due to complexity and high variance of the Doppler spectrum over time, the possible mitigation method will be based on adaptive filtration of the three most dominant spectral components which occurred in the Doppler spectrum.

The novelty of this work is the design of an algorithm for the prediction of the dominant spectral components. This algorithm will be used as an input for the adaptive filtration method of the subsequent influence mitigation of the WTs. The uniqueness of this method is in a pure software solution which does not require any special hardware component and can be integrated to any radar system. The principle of the algorithm is based on the extraction of three dominant spectral components (DSC) from the measured radar data and consequent prediction of these components based on the Unscented Kalman Filter (UKF).

The method prerequisites are as follows: (1) the position of the WT must be known with respect to the radar (for identification of the specific radar cell), (2) aliasing of the Doppler shift caused by WT blade movement should not

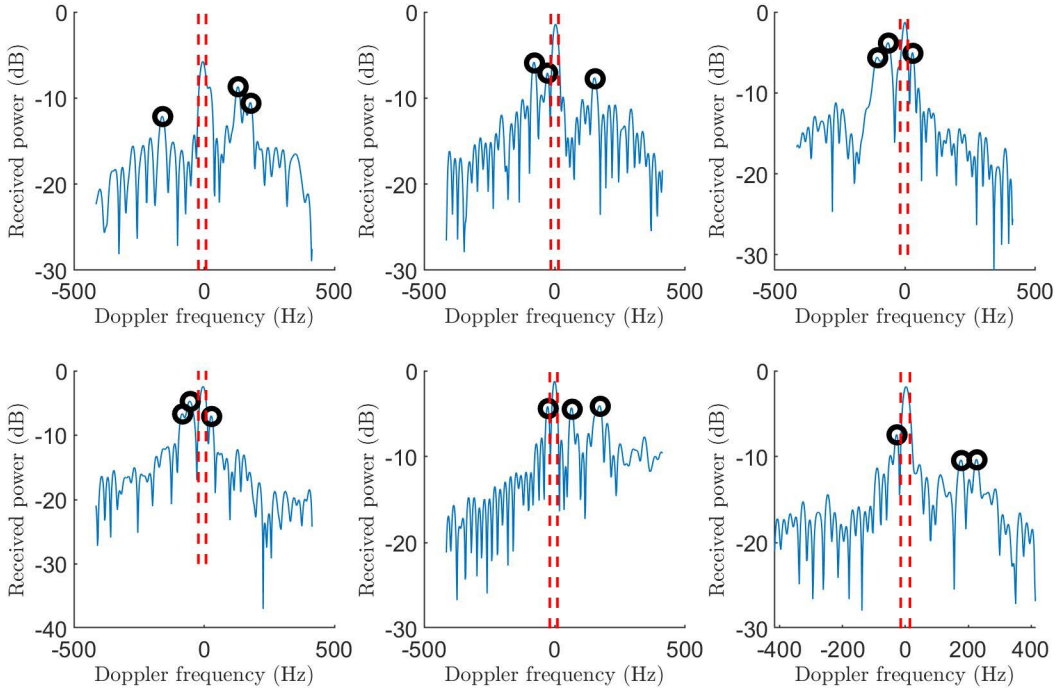

FIGURE 1. Measured doppler spectra of the reflected signal from the WT at variable times with constant time steps. Spectra contains the spectral components from the static part (dashed red lines) and the dominant spectral components from the WT blades (black circles). The spectra are displayed with a time difference of 200 ms. Measurement parameters: central frequency 3 GHz, Pulse repetition frequency (PRF) 1 kHz, Pulse width (PW) 200 ns, and distance between the radar and WT (VESTAS V90) was 420 meters.

occur, (3) only one WT must be present in each resolution cell of the radar. In the case of multiple WTs presented in a single cell, the spectrum contains a multiple of three maxima presented in the Doppler spectrum (each WT produce three maxima).

For a successful design, validation, and testing phase of the UKF-based dominant spectral component prediction method, it is necessary to have a variety of real measurements of signal reflections for the different types of wind turbines under different conditions (such as rotation speed, blade rotation relative to the radar system, etc.). In practice, the implementation of the measurements is very complex, and time and cost consuming. The difficulty of the measurements is mainly due to (1) the unavailability of a suitable location for measuring the reflections from wind turbines (multiple measurements are required for different blade rotations to evaluate the variability of the reflected signal Doppler spectrum), (2) the availability of the signal records with different blade rotation speeds (to evaluate the magnitude of the maximum Doppler shift of the reflected signals), (3) climatic conditions (the functionality of the wind turbines at a given measurement time is not guaranteed in case of moderate wind or no wind), and (4) the high cost of the technical equipment needed for the measurements.

Due to all these reasons, we proposed a model of the reflected signals from wind turbines, which is described in detail in [31], [32], [33], and [34]. The model allows the calculation of reflected signals for input parameters, both from the radar system perspective and wind turbine perspective. The model parameters from the radar perspective are radar system position in Cartesian coordinates, carrier frequency, pulse repetition interval, pulse width, inter-pulse modulation, etc. From the wind turbine perspective, it is the position of the wind turbine(s), the orientation of the WT blade rotation in the direction of the radar system, number of blades, blade rotation speed, number of multipath propagation reflections (up to three reflections), etc. The model outputs are the reflected signals from the wind turbines in the time domain (signal), the Doppler spectrum of the reflected signal, and the evolution of the Doppler spectrum over time (spectrogram). The model of the reflected signals from the WTs was compared with real measurements and confirms a consensus between real and model data.

The UKF-based dominant spectral component prediction method was designed and tested on the real measurements. The model data were used for the determination of the variance of reflected signals for different parameters of the WTs.

The article is organised into five chapters. In the first chapter, we describe the importance of wind turbine mitigation with a review of the current solutions and a novelty description of our approach. The second chapter focuses on the negative effects of the wind turbine on a radar system. Chapter three presents a system description with a focus on the extraction and prediction of the dominant spectral component. Chapter four is devoted to the presentation of the results based on real-measurement from various sites across

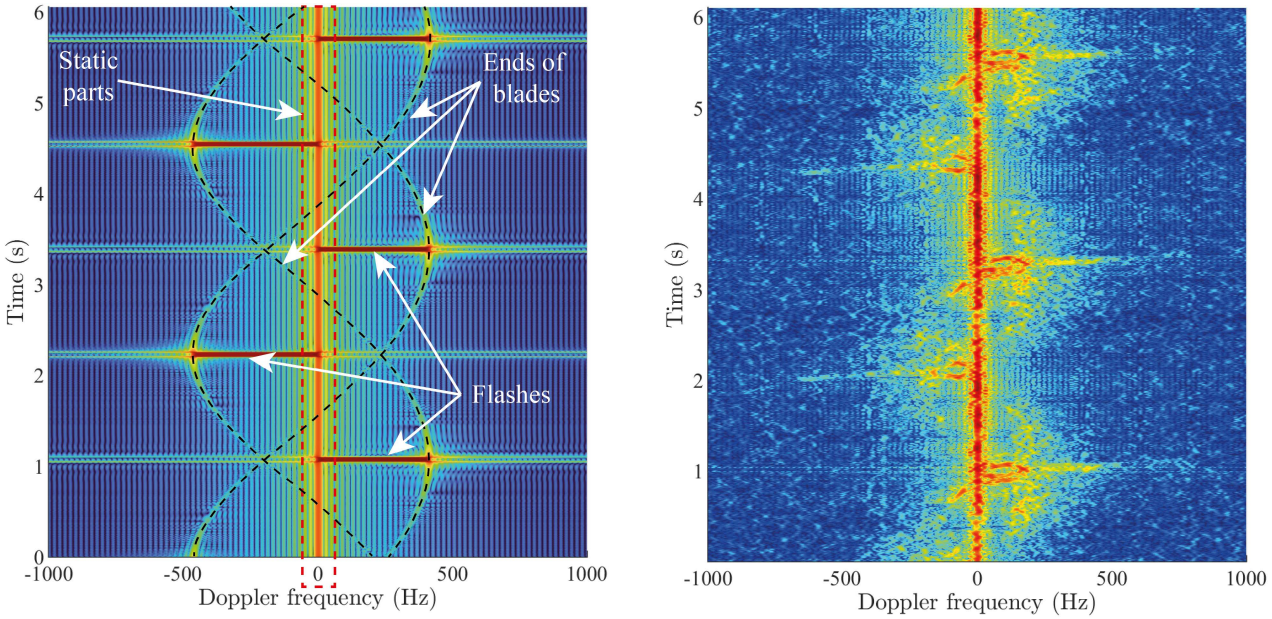

(a) The results of the model together with a description of the individual phenomena (reflections from the blades, flashes).

(b) The Doppler spectrogram of the measured signal.

FIGURE 2. Illustrative view of the comparison of modelled (a) and measured (b) Doppler spectrogram results. The parameters of the measurement are central frequency 3 GHz, Pulse Repetition Frequency (PRF) 1 kHz, Pulse Width (PW) 200 ns. The distance between the radar and WT (VESTAS V90) was 420 meters.

Europe. Chapter five is the conclusion and recommendation for future research.

II. INFLUENCES OF WT ON RADAR SYSTEMS

A typical WT is assembled from a tower, a nacelle, and propeller blades (we consider only the most common three blades WT). The behaviour of the Doppler spectrum of reflected signals from a WT is extremely complex and variable in time. An example of the measured WT Doppler spectra in variable times, with constant time step, is presented in Fig. 1. Considering the high variability of the Doppler spectrum of the reflected signal, it is difficult to obtain a generalized overview of the time evolution of the reflected signal Doppler spectrum behaviour. The better representation of the Doppler spectra evolution is by a spectrogram. In Fig. 2, the left spectrogram shows a modelled output with the same input parameters as the measurement results presented on the right side of Fig. 2 [35], [36].

The reflection of WT influence is divided into two main groups: (1) the reflections caused by WT static parts (tower, nacelle) and (2) reflections caused by WT moving parts (blades). The reflected signals from the static parts of the WTs do not add complexity to the Doppler spectrum and could be considered as part of the ground clutter. The Doppler spectra in Fig. 1 are presented by a dashed red line with zero or small Doppler shift (narrow bandwidth around zero Doppler shift). The small Doppler shift is caused by trembling, or vibration of the WT, which is in turn caused by external influences such as wind. Mitigation of the influences of WT static parts is achieved by the standard ground clutter suppression techniques mentioned earlier. The major problem for the radar system is caused by the moving part of the WT (blades) which causes a significant change in the Doppler spectrum behaviour. Moving parts of a WT contribute to two of the most significant phenomena related to spectrum behaviour: (1) the dominant spectral components, and (2) flashes. The first phenomenon is presented by the three dominant spectral components caused by the end of the WT blades (the highest tangential speed). Dominant spectra components depend mainly on the rotation of the blades (position and amplitude of the dominant spectral component), length of the blades, WT rotation speed of the blades, and yaw rotation of the radar system with respect to the WT blades. The time evolution signature is characterized by the three sinusoidal waveforms presented in Fig. 2 (left by black dashed lines). Each sinewave corresponds to the individual blade. The maxima of the sinewaves match the dominant spectral component, presented in Fig. 1 by the black circles. The waveforms have the same amplitude, the same frequency, and are phase-shifted by $2\pi/3$, i.e., corresponding to the angle between blades, being 120°. The second phenomenon that occurs only under specific conditions is called "flash". The origin of the flashes occurs when the position of one of the WT blades is perpendicular to the propagating transmitted wave. In this case, the transmitted signal is in phase with the blade and produces a very strong reflection containing Doppler frequencies in the whole range from 0 Hz to the maximum positive/negative dominant Doppler shift. Flashes cause complete obscuration of the half-width of the Doppler spectrum in the positive or negative part. The flashes will have

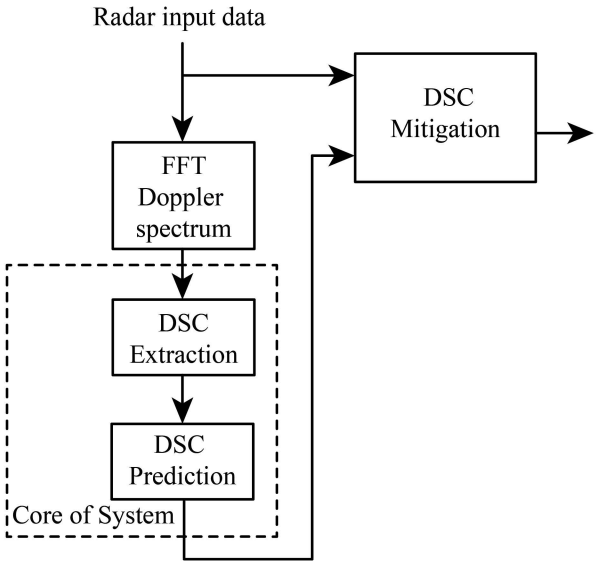

FIGURE 3. A block diagram of the mitigation system. The extraction and prediction of DSC present the core of the system. The paper focuses only on the extraction and prediction of DSC.

a significant effect on the impact of the radar system detection capability. At the same time as flashes occur, the Doppler shifts of the other two blades are overlapped simultaneously. The duration of the flashes is periodically repeated, and the typical duration is in the order of ms (typical 10-20 ms or 2-4% of blades rotation) before the blade is rotated by an angle of $\Delta\varphi \sim \lambda/L$, where λ is a wavelength, and L is the length of the WT blade. These flashes are very difficult to suppress by any mitigation method of the received signal due to the high amplitude of the reflection and the large bandwidth of the Doppler frequencies that occupy the whole half-bandwidth of the radar system. The flashes are presented in Fig. 2 (left – model, right – measurement).

III. SYSTEM DESCRIPTION

The principle of the system for mitigating WT influences on a radar system, is based on DSC extraction and prediction, and these two operations present the core of the system. The predicted values of the DSCs are used for consequent mitigation of the DSC in radar signal. Mitigation techniques are generally based on adaptive filtration methods [37], [38]. The block scheme of the system is presented in Fig. 3. The DSC extraction and prediction, due to high variability of the input signal Doppler spectrum behaviour, is an extremely complicated problem. Therefore, the paper focuses only on DSC extraction and prediction operations.

A. DSC EXTRACTION

For the DSC extraction, the Automatic Multiscale-based Peak Detection (AMPD) algorithm is used. The primary objective of this algorithm is to identify the three DSCs in the Doppler spectrum. DSCs are presented by the three sinusoidal waveforms with the same amplitude and frequency, and they are

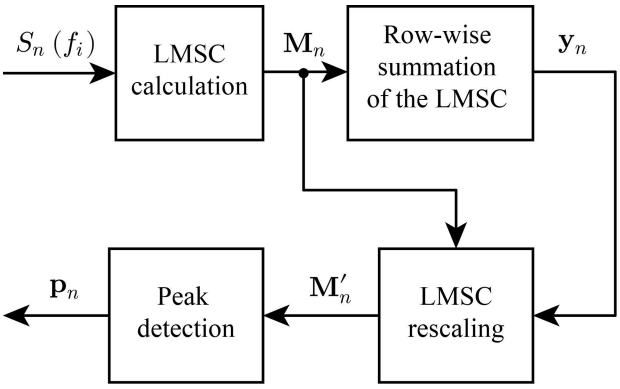

FIGURE 4. A block diagram of the AMPD algorithm for finding peaks, i.e., dominant spectral components in the doppler spectrum of input radar data. This algorithm is appropriate and effective even in noisy environments where standard methods fail.

phase-shifted by $2\pi/3$. Their sum is equal to zero. The two DSCs are extracted from the Doppler spectra, and the third DSC is consequently computed.

The block diagram of the AMPD algorithm is shown in Fig. 4. The input of the AMPD algorithm is the Doppler spectrum $S_n(f_i)$ for the n-th line of the spectrogram, where f_i is the discrete Doppler frequency for index i in the interval 1 to N, and N is the length of the FFT (Fast Fourier Transform). Each slice of the spectrogram is computed typically from 10-40 Pulse repetition periods (PRP). The first step of the AMPD algorithm is the calculation of the local maximum scalogram (LMSC). The output of this computation is a matrix $\mathbf{M}_n$, whose elements are given by

$$m_{k,i} = \begin{cases} 0, & S_n(f_{i-1}) > S_n(f_{i-k-1}) \wedge \\ & S_n(f_{i-1}) > S_n(f_{i+k-1}) \\ p, & \text{otherwise}, \end{cases} \tag{1}$$

where p is a uniformly distributed random number between 1 and 2, and $k = 1, \ldots, L$, where $L = \lceil N/2 \rceil - 1$. The second step is the row-wise summation of the matrix $\mathbf{M}_n$, which is given by

$$y_k = \sum_{i=1}^{N} m_{k,i}. \tag{2}$$

The vector $\mathbf{y}_n$, containing y_k elements, represents information about all local maxima. The global minimum of the $\mathbf{y}$ vector can be expressed as a $\eta = \min(y_k)$, which gives us the scale with the most local maxima. In the third step of the algorithm, the matrix $\mathbf{M}_n$ is reduced to the matrix $\mathbf{M}'_n$ which contains only the elements $m_{k,i}$ that satisfy the condition $k < \eta$. The matrix $\mathbf{M}'_n$ has a reduced dimension $\eta \times N$. In the last step (peak detection block), the vector of standard deviations σ_i of the $\mathbf{M}'_n$ matrix individual columns are given by

$$\sigma_i = \sqrt{\frac{1}{\eta - 1} \sum_{k=1}^{\eta} \left(m_{k,i} - \frac{1}{\eta} \sum_{k=1}^{\eta} m_{k,i} \right)^2}. \tag{3}$$

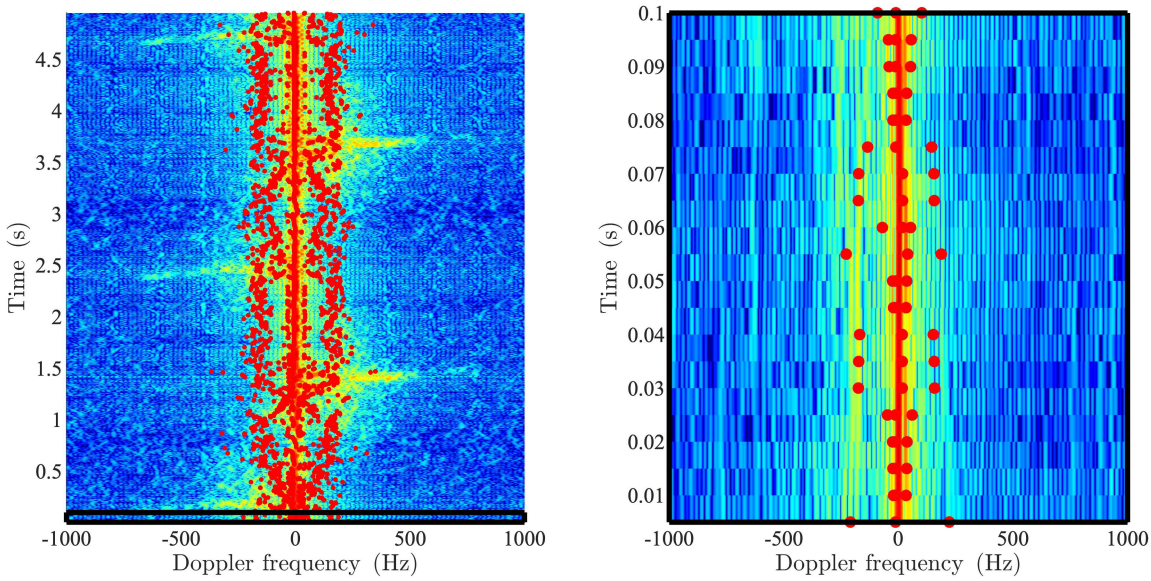

FIGURE 5. The result of the AMPD algorithm used for extraction of DSC are highlighted by red points (left). The black box in the spectrogram on the left represents the area that has been zoomed in on the right side. The red dots in both figures represent the extracted DSCs.

The vector of peaks $\mathbf{p}_n$ can be found at the positions, where the standard deviations σ_i are zero. In the vector of peaks $\mathbf{p}_n$, the two most dominant (two DSC) are selected and the third DSC is calculated with condition that the sum of all three DSCs has to be zero. More detailed information about the AMPD algorithm is described in [39].

The example of the data with extracted DSC are shown in Fig. 5. The red points represent the extracted DSC. This extracted data is used as the input of the prediction algorithm.

B. DSC PREDICTION USING UKF

To estimate the DSC data, the Kalman filtering approach was used. The Kalman filter exists in several variants, such as conventional Kalman Filter (KF), Extended (EKF), Unscented (UKF), Simplified (SKF), and Central difference (CDKF), which are described in [40], [41], [42], and [43].

Due to the nonlinear behaviour of the DSC, we are not able to use conventional KF. The measurement model requires linearized KF modification, EKF or UKF. We have selected UKF providing higher accuracy at the cost of higher complexity. This increased complexity is caused by the calculation of the covariance matrix in multiple sigma points. Sigma points (6) are computed by Cholesky factorization. The discussion of numerical complexity and accuracy of the different versions of KF can be found e.g. in [43], [44], and [45].

In general, the main difference between the EKF and the UKF is the model linearisation method. This method is essential for KF modifications. The EKF linearizes the model based only on its mean value using the Taylor expansion. In contrast, the linearisation of a model in UKF is performed on multiple points depending on the number of input states. Such points are known as sigma points χ.

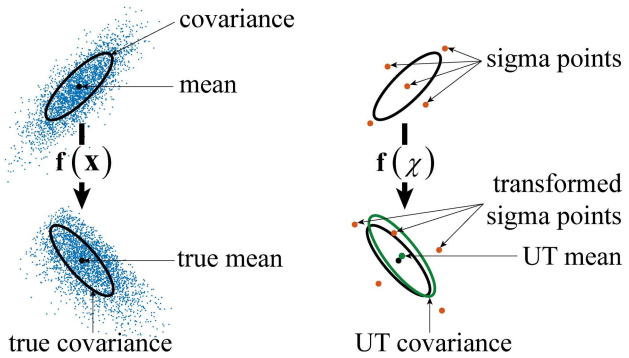

FIGURE 6. Graphical representation of the idea of UKF sigma points. From the transformed sigma points, both the mean and covariance of the gaussian distribution are calculated.

In UKF, the linearisation is done using $2L+1$ sigma points. The variable L denotes the number of states. In our case, $L = 3$ and corresponds to the amplitude, frequency, and phase of the DSC. The linearisation is therefore performed using 7 points. The first point corresponds to the mean value of the model distribution, and the other points are distributed along the axes of an ellipsoid. Their position is described in equation (3). The principle is shown graphically in Fig. 6. The left side of the image illustrates the situation of the nonlinear function $\mathbf{f}$ that transforms the mean and covariance. In contrast, the right side illustrates the UKF situation. For this situation, the sigma points are selected and converted into transformed sigma points using UT (uncentered transformation). From the transformed sigma points, both the mean and covariance of the Gaussian distribution are calculated. It can predict the following states based on the transformed mean

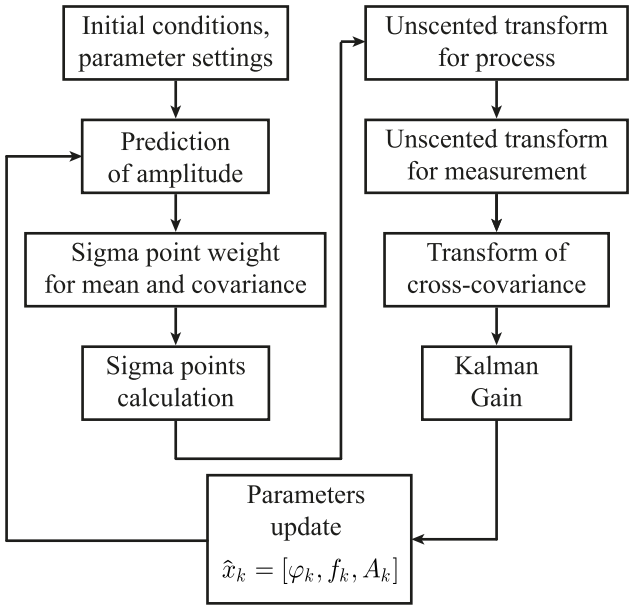

FIGURE 7. Complete block diagram of UKF prediction algorithm. It contains all the essential parts of the algorithm including setting of the initial conditions, calculation of sigma points, UT for process, UT for measurement, Kalman gain calculation, and parameter update (phase, frequency and amplitude of DSC sine waveforms).

and covariance, which are close to non-Gaussian (nonlinear) distributions. Fig. 7 illustrates a block diagram of the UKF algorithm. This algorithm is comprised of several basic steps.

First, initial conditions are defined, which correspond to the initial states $\hat{\mathbf{x}}_0 = [\varphi_0, f_0, A_0]$, where φ_0 is the initial phase of the sinusoidal extracted DSC waveforms, f_0 is the frequency of sinusoidal waveforms, and A_0 is the amplitude of the sinusoidal waveforms. Another condition is the initial covariance matrix of the states, which was chosen to be $\mathbf{P}_0 = \mathbf{I}$, where $\mathbf{I}$ is a unit matrix with dimension $L \times L$. The noise process covariance $\mathbf{Q}$ is given by

$$\mathbf{Q} = \begin{pmatrix} \frac{T_s^3\sigma_1}{3} & \frac{T_s^2\sigma_1}{2} & 0 \\ \frac{T_s^2\sigma_1}{2} & T_s\sigma_1 & 0 \\ 0 & 0 & T_s\sigma_2 \end{pmatrix}, \tag{4}$$

where T_s is the sampling period, σ_1 is the standard deviation of the process error for phase and frequency, and σ_2 is the standard deviation of the process error for amplitude. The measurement covariance matrix is $\mathbf{R} = r\mathbf{I}$, where r is the standard deviation of the measurement error.

The next part of the algorithm focuses on calculating the weights of the sigma points, which are the same throughout the algorithm. The weights are calculated separately for the mean $\mathbf{W^m}$ and for the covariance $\mathbf{W^c}$. Their calculation is given by

$$\mathbf{W}_0^{\mathbf{m}} = \frac{\zeta}{L+\zeta}$$
$$\mathbf{W}_0^{\mathbf{c}} = \frac{\zeta}{L+\zeta} + \left(1 - \alpha^2 + \beta\right)$$
$$\mathbf{W}_i^{\mathbf{m}} = \mathbf{W}_i^{\mathbf{c}} = \frac{1}{2\,(L+\zeta)}, \quad \text{for } i = 1, \ldots, 2L, \tag{5}$$

where the scaling factor ζ tells us how far away from the mean the remaining sigma points will be placed, and is defined as $\zeta = \alpha^2\,(L+\kappa) - L$. Variables α, κ are adjustable parameters that allow us to customize the behaviour of the UKF. Variable $\beta = 2$ is the most appropriate setting for a Gaussian distribution. In our case, the parameters α and κ were set to 0.01.

Initially, the amplitude prediction utilises the properties of a sum of three sinusoidal waveforms, phase shifted by $2\pi/3$ radians. Detailed descriptions can be found in [46].

The next step is the calculation of the sigma points $\boldsymbol{\chi}_{k-1}$, and this is given by

$$\begin{aligned} \boldsymbol{\chi}_{k-1}^0 &= \hat{\boldsymbol{x}}_{k-1} \\ \boldsymbol{\chi}_{k-1}^i &= \hat{\boldsymbol{x}}_{k-1} + \left(\sqrt{(L+\lambda)\,\mathbf{P}_{k-1}}\right)_i, \\ &\quad \text{for } i = 1, \ldots, L \\ \boldsymbol{\chi}_{k-1}^i &= \hat{\boldsymbol{x}}_{k-1} - \left(\sqrt{(L+\lambda)\,\mathbf{P}_{k-1}}\right)_{i-L}, \\ &\quad \text{for } i = L+1, \ldots, 2L, \end{aligned} \tag{6}$$

where $\hat{\boldsymbol{x}}_{k-1}$ is the mean of the states in $k-1$, and $\mathbf{P}_{k-1}$ is the covariance matrix of the states in $k-1$. Computed sigma points are used for the UT (Unscented transform), which is given by

$$\begin{aligned} \mathbf{X}_{k|k-1} &= f\left(\boldsymbol{\chi}_{k-1}\right) \\ \hat{\mathbf{x}}_k' &= \hat{\mathbf{x}}_{k-1} + \mathbf{W^m}\mathbf{X}_{k|k-1} \\ \Delta\mathbf{X}_{k|k-1} &= \mathbf{X}_{k|k-1} - \underbrace{\left[\hat{\mathbf{x}}_k', \ldots, \hat{\mathbf{x}}_k'\right]}_{2L+1 \text{ times}} \\ \mathbf{P}_{\hat{\mathbf{x}}_k,\hat{\mathbf{x}}_k} &= \Delta\mathbf{X}_{k|k-1}\mathrm{diag}\left(\mathbf{W^c}\right)\Delta\mathbf{X}_{k|k-1}^T + \mathbf{Q}, \end{aligned} \tag{7}$$

where $\mathbf{X}_{k|k-1}$ is the transformed sigma points using the process function $f(.)$, $\hat{\mathbf{x}}_k'$ is the change of the previous state depending on the transformed sigma points $\mathbf{X}_{k|k-1}$ and the mean value weights $\mathbf{W^m}$, $\Delta\mathbf{X}_{k|k-1}$ is the change of the transformed sigma points and $\mathbf{P}_{\hat{\mathbf{x}}_k,\hat{\mathbf{x}}_k}$ is the covariance of the posterior sigma points for the process.

The UT for the measurement is performed in the same way and is given by

$$\begin{aligned} \mathbf{Z}_{k|k-1} &= h\left(\boldsymbol{\chi}_{k-1}\right) \\ \hat{\mathbf{z}}_k' &= \hat{\mathbf{z}}_{k-1} + \mathbf{W^m}\mathbf{Z}_{k|k-1} \\ \Delta\mathbf{Z}_{k|k-1} &= \mathbf{Z}_{k|k-1} - \underbrace{\left[\hat{\mathbf{z}}_k', \ldots, \hat{\mathbf{z}}_k'\right]}_{2L+1 \text{ times}} \\ \mathbf{P}_{\hat{\mathbf{z}}_k,\hat{\mathbf{z}}_k} &= \Delta\mathbf{Z}_{k|k-1}\mathrm{diag}\left(\mathbf{W^c}\right)\Delta\mathbf{Z}_{k|k-1}^T + \mathbf{R}, \end{aligned} \tag{8}$$

where $\mathbf{Z}_{k|k-1}$ are the transformed sigma points using the measurement function $h(.)$, $\hat{\mathbf{z}}_k'$ is the change in the prior state depending on the transformed sigma points $\mathbf{Z}_{k|k-1}$ and the mean value weights $\mathbf{W^m}$, $\Delta\mathbf{Z}_{k|k-1}$ is the change in the transformed sigma points, and $\mathbf{P}_{\hat{\mathbf{z}}_k,\hat{\mathbf{z}}_k}$ is the covariance of the posterior sigma points for the measurement.

Once the dependencies between the measurement and the process are known calculation of the cross-covariance matrix

TABLE 1. Information on the four measurement stations where the measurements were made. Data includes station position, WT type, and distance between measuring station and WT.

GPS position of measurement site	GPS position of the WT	Site	WT type	Distance between WT and MS	Tower height	Blade length	Maximum rotation speed
49.729333N 15.503056E	49.726389N 15.506944E	Kamen (Czech Republic)	Vestas V90 [47]	420 m	80 m	45 m	14.9 rpm
49.4763944N 16.8361E	49.477290N 16.848708E	Protivanov (Czech Republic)	Repower MD77 [48]	910 m	85 m	38.5 m	17.3 rpm
48.426911N 16.636024E	48.434934N 16.644383E	Groß-Schweinbarth 1 (Austria)	Vestas V150 [49]	1029 m	166 m	75 m	12 rpm
48.441548N 16.659965E	48.434934N 16.659965E	Groß-Schweinbarth 2 (Austria)	Vestas V150 [49]	1322 m	166 m	75 m	12 rpm

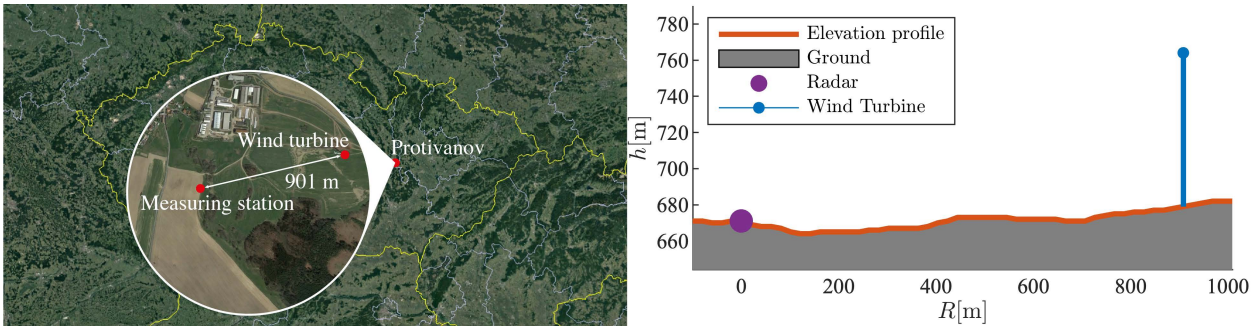

FIGURE 8. Map of the approximate position of the village of Protivanov in the Czech republic where the measuring station and WT are enlarged. The distance from each other is approximately 901 meters. The right picture shows the terrain profile between measuring station and wind turbine.

of the process and measurement $\mathbf{P}_{\hat{\mathbf{x}}_k,\hat{\mathbf{z}}_k}$ is required, and is given by

$$\mathbf{P}_{\hat{\mathbf{x}}_k,\hat{\mathbf{z}}_k} = \Delta\mathbf{X}_{k|k-1}\text{diag}\left(\mathbf{W}^{\mathbf{c}}\right)\Delta\mathbf{Z}^T_{k|k-1}. \tag{9}$$

From the knowledge of the cross-covariance, it is possible to compute the so-called Kalman gain $\mathbf{K}_k$. The Kalman gain tells us which part (process or measurement) can be trusted more. This then becomes an important component for updating the future states and the covariance matrix, which in turn becomes the future input values for the next iteration of the algorithm. The Kalman gain is given by

$$\mathbf{K}_k = \mathbf{P}_{\hat{\mathbf{x}}_k,\hat{\mathbf{z}}_k}\mathbf{P}^{-1}_{\hat{\mathbf{z}}_k,\hat{\mathbf{z}}_k}. \tag{10}$$

For us, the state updates and the corresponding covariance matrices are predictions of the future parameters of the DSC sine waveforms (updated parameters represent the new values of phase φ, frequency f and amplitude A of the DSC sine waveforms), and their computation is given by

$$\begin{aligned}\hat{\mathbf{x}}_k &= \hat{\mathbf{x}}'_k\mathbf{K}_k\left(\mathbf{z}_k - \hat{\mathbf{z}}'_k\right)\\ \mathbf{P}_k &= \mathbf{P}_{\hat{\mathbf{x}}_k,\hat{\mathbf{x}}_k} - \mathbf{K}_k\mathbf{P}^T_{\hat{\mathbf{x}}_k,\hat{\mathbf{z}}_k},\end{aligned} \tag{11}$$

where $\mathbf{z}_k$ are the extracted DSCs in k-th. Parameter estimation of the UKF and its variations are described in [50] and [51]. After this update, the algorithm repeats. In the following section, DSC prediction results, from real measurements, are presented.

IV. RESULTS AND DISCUSSION

The DSC extraction and prediction algorithm was validated on real measured radar data sets. The radar data was collected at various sites and for various types of the WTs in Czech Republic and Austria. Information about sites is shown in Tab. 1. The example of the of the terrain profile and measurement site for Protivanov is shown in Fig. 8. Consequently, the measured RAW data was pre-processed to the format suitable for the designed extraction/prediction algorithm. For the data collection it was necessary to design a measurement chain of the reflected WT signals, which is described below.

A. MEASUREMENT CHAIN

The block diagram of the designed measurement system is shown in Fig. 9. The core of the system is presented by the Software-Defined Radio (SDR) from National Instruments [52]. The SDR model is USRP-2954 that is controlled by a PC and high-speed data SSD storage. The SDR contains transmitting (TX) and receiving (RX) modules connected to parabolic antennas JRMC–1200-2.9 MIMO [53]. The transmitting and receiving antennas are the same (with identical specifications). The antennas are physically separated to protect the receiver from the transmitter's power. Between the antennas, insulation of around 60-70 dB, could be achieved. Through link budget analysis, it was necessary to use sufficient transmit power to ensure that the received signal was above the noise level. Thus, a broadband power amplifier ZHL-16W-43-S+ [54] was connected to the transmitting side of SDR. On the receiver side, an appropriate bandpass

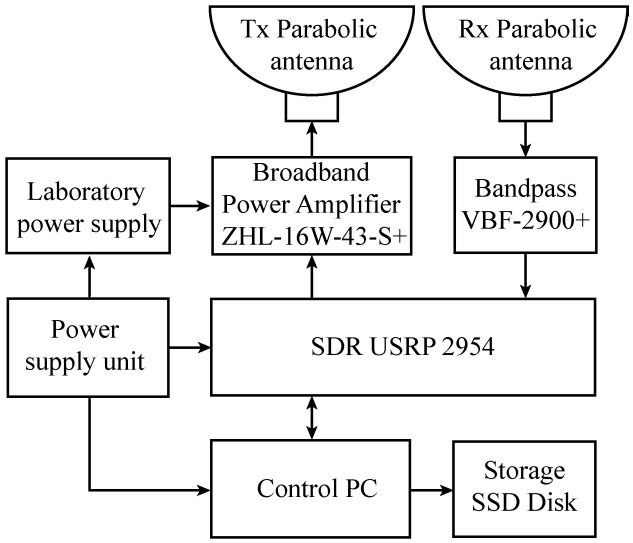

FIGURE 9. Block diagram of measurement chain that contains an SDR USRP-2954 with a transmitting/receiving module, power amplifier of the input signal, identical transmitting and receiving parabolic antenna, and bandpass filter. The SDR is controlled by the PC with a high-speed SSD disk.

filter (type VBF-2900+) was connected to the output of the antenna to limit the bandwidth of the received signal. The received signal was demodulated and pre-processed to extract the I/Q (In-phase and Quadrature components) components of the received signal. The I/Q data was stored on an SSD Disk. The SDR was controlled by GNURadio 3.8.4.0 [55], which runs on a Linux operating system based on the Ubuntu distribution. Since this is an outdoor measurement, it was necessary to use a portable generator to power the system's components.

With the respect to the maximal Doppler shift caused by the WT blades, and maximal recording speed of the SSD drive, the measurement parameters was set up as follows: Carrier frequency of the SDR $f_c = 3$ GHz, sampling frequency $f_s = 40$ MHz, PRF 1-1,25 kHz, pulse width 200 ns, and transmitted power 32 dBm. Several measurements were performed at each site. Simultaneously, videos of the WTs for collection of the real-time WT parameters were recorded (WT rotation speed, orientation of the WT blades with respect to the central axis of the transmitting and receiving antenna). Due to the parabolic antennas' ability to change a polarization (horizontal, vertical, and cross-polarization) several measurements for each polarization were obtained. By virtue of the fact that SDR buffer size was limited, maximal time length of the individual records was restricted to twenty seconds.

B. DSC PREDICTION AND RESULTS

The raw measured data was processed offline and all necessary pre-computation, data operation and outputs (such as Doppler spectra, spectrogram) were performed in MATLAB software [56]. The pre-processed data represent an input data of the mitigation system shown in Fig. 3. The example of the typical spectrogram from the locality of Groß-Schweinbarth, for different polarisation, is shown in Fig. 10.

TABLE 2. Results of the DSC prediction containing mean DSC prediction, and percentage DSC prediction error for various sites. Dataset numbers (for ease of reference), measurement locations and polarizations used are listed.

Dataset no.	Site	Polarization	Mean prediction error [Hz]	Percentage prediction error [%]
M01	Kamen	Horizontal	24.17	1.61
M02	Kamen	Vertical	25.37	1.59
M03	Kamen	Vertical	16.92	1.13
M04	Kamen	Horizontal	13.11	1.25
M05	Kamen	Horizontal	34.07	3.10
M06	Kamen	Horizontal	43.96	3.67
M07	Groß-Schweinbarth 1	Horizontal	79.32	3,17
M08	Groß-Schweinbarth 1	Horizontal	70.08	2.80
M09	Groß-Schweinbarth 1	Vertical	73.33	2.93
M10	Groß-Schweinbarth 1	Cross	21.29	1.42
M11	Groß-Schweinbarth 2	Vertical	47.18	1.89
M12	Groß-Schweinbarth 2	Vertical	43.58	1.74
M13	Groß-Schweinbarth 2	Horizontal	20.46	0.82
M14	Protivanov	Vertical	21.85	0.87
M15	Protivanov	Vertical	27.77	1.26
M16	Protivanov	Horizontal	18.81	0.85

All measured datasets were processed by the extraction and prediction part of the mitigation algorithm and the results are presented in Tab. 2. Tab. 2 includes information parameters: Number of measurements, site name, polarization setting, and the results part of the DSC prediction. The DSC prediction evaluation is based on the mean prediction error and consequent percentage prediction error. The mean prediction error indicates how different, on average, the predicted DSC value is from the actual extracted DSC. Given measurements at multiple locations with different WTs under different weather conditions, the percentage error of the DSC prediction needs to be calculated relative to the maximum possible DSC in that region. The maximum possible DSC depends on many factors including the carrier frequency and geometry of the WT.

The typical result of the three highest spectral components of the real data and predicted DSC values is shown in Fig. 11. In each instant time value, the graph shows three extracted components (orange circles) and three predicted values by the designed algorithm (blue points). The presented results are from the locality of Kamen (dataset M04). A zoomed graph for the defined time interval is also shown for a more detailed illustration. The trend of the DSC prediction error for dataset

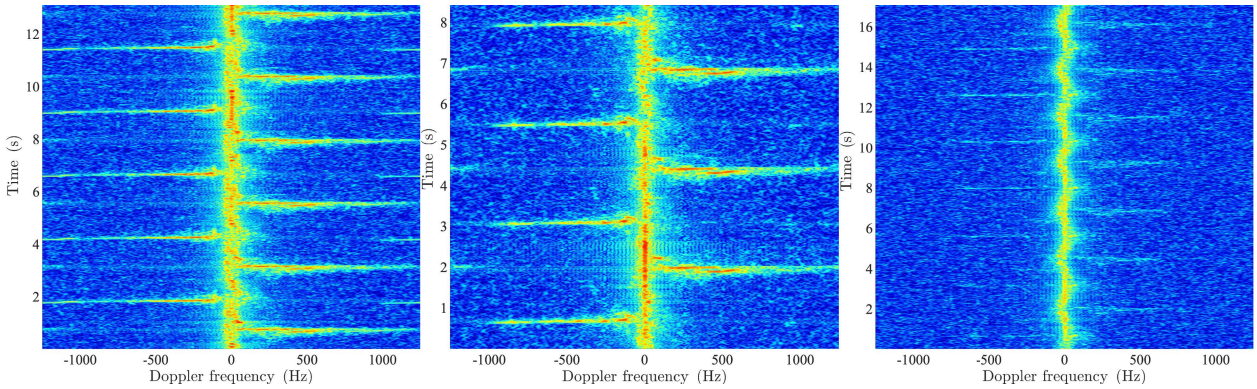

FIGURE 10. The example of the spectrogram for horizontal (left), vertical (middle), and cross-polarization (right) of the measured data from Groß-Schweinbarth locality. The change in polarization affects the shape of the spectrogram, as can be seen in these three examples.

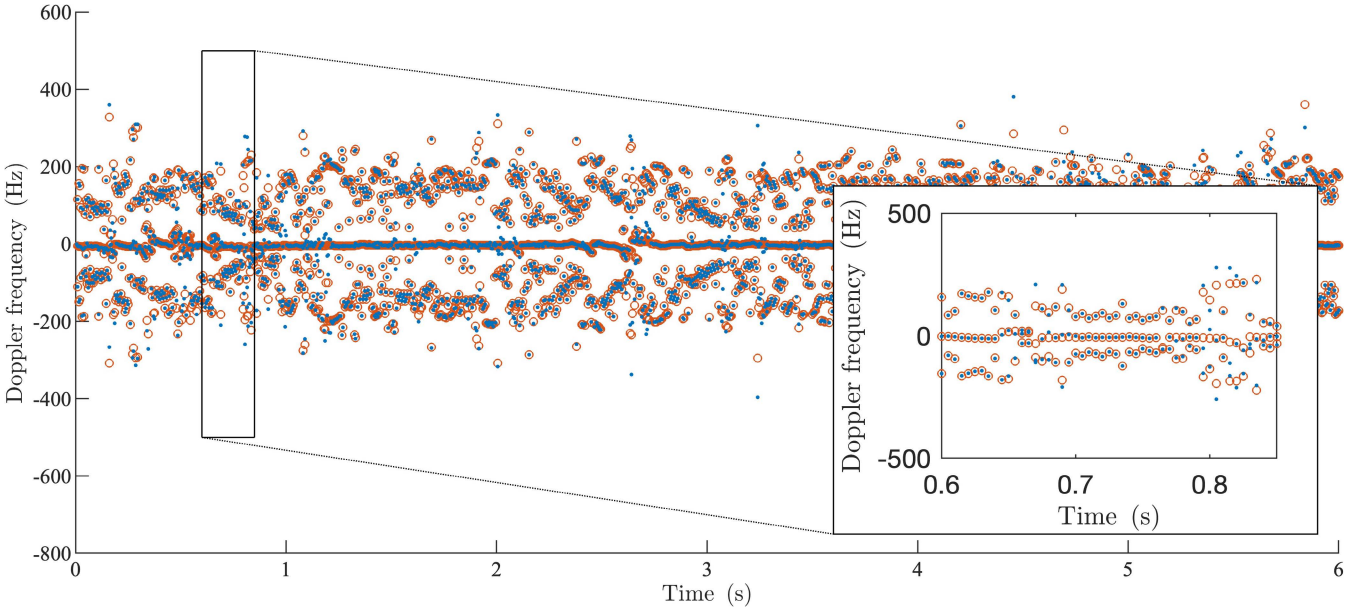

FIGURE 11. Measurement dataset M04-DSC prediction behaviour graph and zoomed time-bounded graph. Orange circles and blue dots correspond to the extracted DSC from measurements and predicted DSC, respectively.

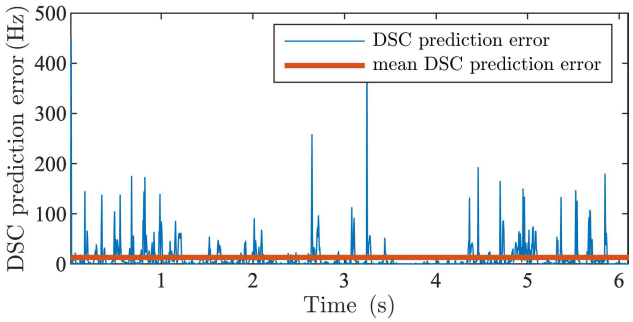

FIGURE 12. Measurement dataset M04-DSC prediction error behaviour graph (blue line) calculation of the mean DSC prediction error (orange line).

M04 (blue line) is presented in Fig. 12. This DSC prediction error is a sum of all three differences between predicted DSCs and extracted DSCs. The calculated average DSC prediction error (orange line) is also shown. For this case, the mean value of the DSC prediction error comes out to be approximately 13.11 Hz, and the standard deviation is 30.80 Hz.

According to Tab. 2, the results can be assessed in terms of several approaches. On close examination, we find that the highest percentage error in DSC prediction occurred at both measurement sites in the Groß-Schweinbarth region. The main reason for exaggerated error is that the largest WT of the three types (Vestas V150) was used in the measurements. This WT produced the most significant Doppler shift, hence the highest WT prediction error occurred here. Another influence on WT prediction accuracy is the choice of polarization. When vertical polarization is utilized the "flash" phenomenon is significant in the Doppler spectrum compared to other polarizations. The phenomenon causes fluctuation in DSC, and for that reason, vertical polarization corresponds

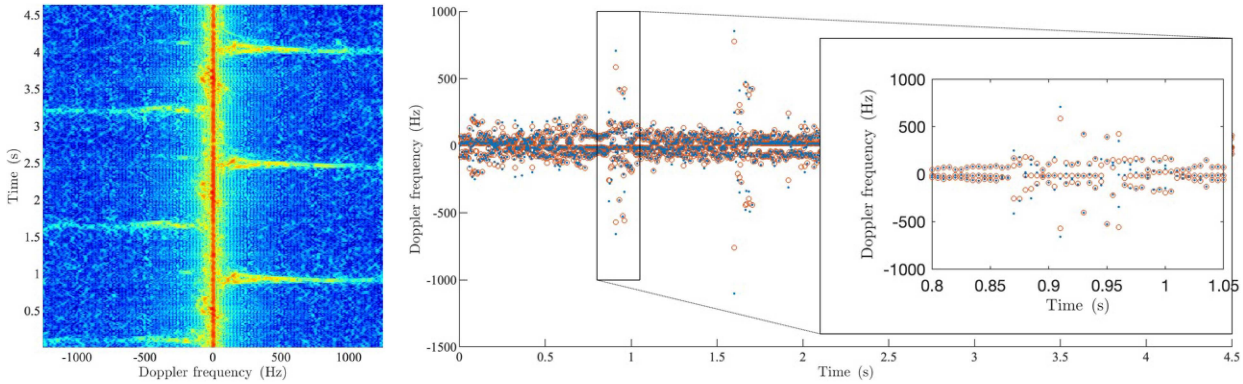

FIGURE 13. (left) Doppler spectrogram for measurement dataset M17 from Protivanov locality (Vertical polarization). (right) DSC prediction behaviour graph and zoomed time-bounded graph. Orange circles and blue dots correspond to the extracted DSC from measurements and predicted DSC, respectively.

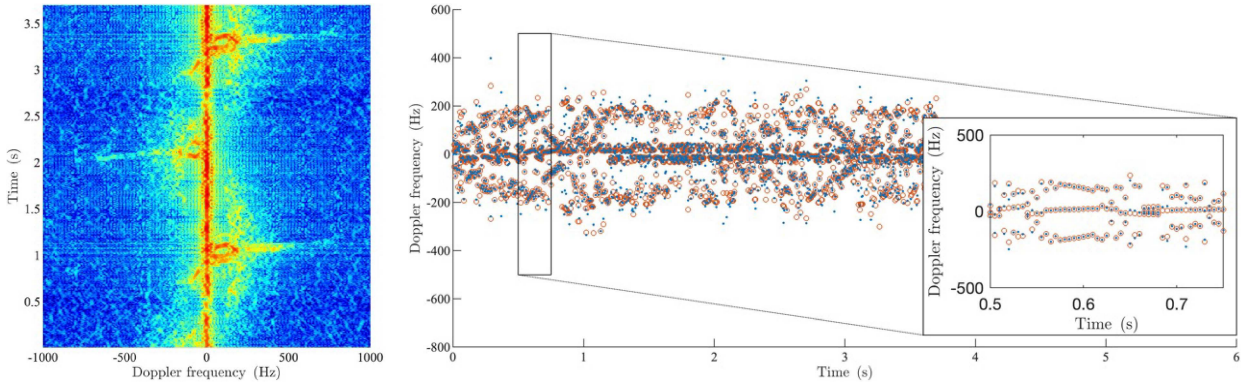

FIGURE 14. (left) Doppler spectrogram for measurement dataset M05 from Kamen locality (Horizontal polarization). (right) DSC prediction behaviour graph and zoomed time-bounded graph. Orange circles and blue dots correspond to the extracted DSC from measurements and predicted DSC, respectively.

to a decreased DSC prediction accuracy (Fig. 13). The flash is less evident when using horizontal polarization instead of vertical polarization. Therefore, the DSC prediction fluctuates less in comparison with vertical polarization (Fig. 14). However, the mean DSC prediction error for both polarizations (vertical, horizontal) is similar due to a large number of other aspects (weather conditions, topography of the land, parameters of radar system etc.). If cross-polarization is used, the phenomena of DSC and ''flash'' is not greatly significant, and the prediction accuracy is highest for these three options. The reflection of the radar signal from the WT blades is reduced, and the Doppler shift itself is indistinguishable and easy to predict and mitigate. Overall, the maximum percentage error in DSC prediction for the measured data sets was about 3.7 percent of the maximum possible DSC that the WT could have caused. The measured datasets were in different regions and environments for different types of WT, and yet the DSC prediction accuracy achieved was precise.

V. CONCLUSION

As a result of the work presented in this paper, a new algorithm has been developed for the prediction and tracking of DSC in radar echoes that are corrupted with WT clutter. In our algorithm, we use the unscented Kalman filter (UKF) as the tracking filter. The effectiveness of our algorithm has been demonstrated by tracking DSC in real-radar data. During our research, we have demonstrated that the algorithm is able to work on radar data collected from a variety of different locations. Different antenna polarizations can also be accommodated by the algorithm. In our future research, the predicted DSC will be used as inputs to adaptive filters so that we can effectively mitigate the WT clutter from radar signals.

REFERENCES

[1] B. Gallardo-Hernando, F. Prez-Martnez, and F. Aguado-Encabo, ''Wind turbine clutter,'' in *Radar Technology*, Rijeka, Croatia: InTech, 2010, pp. 87–104.

[2] W. Hall, M. A. Rico-Ramirez, and S. Krämer, ''Offshore wind turbine clutter characteristics and identification in operational C-band weather radar measurements,'' *Quart. J. Roy. Meteorological Soc.*, vol. 143, no. 703, pp. 720–730, Jan. 2017, doi: 10.1002/qj.2959.

[3] W.-Q. Wang, ''Detecting and mitigating wind turbine clutter for airspace radar systems,'' *Sci. World J.*, vol. 2013, pp. 1–8, Dec. 2013, doi: 10.1155/2013/385182.

[4] B. M. Isom, R. D. Palmer, G. S. Secrest, R. D. Rhoton, D. Saxion, T. L. Allmon, J. Reed, T. Crum, and R. Vogt, ''Detailed observations of wind turbine clutter with scanning weather radars,'' *J. Atmos. Ocean. Technol.*, vol. 26, no. 5, pp. 894–910, May 2009, doi: 10.1175/2008JTECHA1136.1.

[5] S. M. Torres and D. A. Warde, "Ground clutter mitigation for weather radars using the autocorrelation spectral density," *J. Atmos. Ocean. Technol.*, vol. 31, no. 10, pp. 2049–2066, Oct. 2014, doi: 10.1175/JTECH-D-13-00117.1.

[6] M. A. Richards, *Fundamentals Radar Signal Processing*, 3rd ed. New York, NY, USA: McGraw-Hill, 2022.

[7] J. Klintberg, T. McKelvey, and P. Dammert, "Mitigation of ground clutter in airborne bistatic radar systems," in *Proc. IEEE 11th Sensor Array Multichannel Signal Process. Workshop (SAM)*, Jun. 2020, pp. 1–5, doi: 10.1109/SAM48682.2020.9104314.

[8] J. T. Peltier, "A study of ground clutter supression at the chill Doppler weather radar," M.S. thesis, Illinois State Water Surv., Univ. Illinois Urbana-Champaign, Champaign, IL, USA, 1989.

[9] S. M. Torres and D. S. Zrnic, "Ground clutter canceling with a regression filter," *J. Atmos. Ocean. Technol.*, vol. 16, pp. 1364–1372, 1999, doi: 10.1175/1520-0426(1999)016<1364:GCCWAR>2.0.CO;2.

[10] P. Gilman. (2020). Offshore Wind Turbine Radar Interference Mitigation (WTRIM) Series: Air Traffic Control Terminal Radar. Department of Energy. Accessed: Sep. 10, 2022. [Online]. Available: https://www.energy.gov/sites/prod/files/2020/11/f80/offshore-wind-turbine-radar-interference-mitigation-webinar-10-26-2020.pdf

[11] C. A. Jackson. Wind Farms and Radars Living Together? International Airport Review. Accessed: Sep. 7, 2022. [Online]. Available: https://www.internationalairportreview.com/article/12201/wind-farms-and-radars-living-together/

[12] S. Moore. World's Largest Offshore Wind Farm: Dogger Bank. Azocleantech. Accessed: Sep. 7, 2022. [Online]. Available: https://www.azocleantech.com/article.aspx?ArticleID=1072

[13] Airport Technology. *Glasgow Airport Installs New Radar to Pave Way for New Wind Farm*. Accessed: Sep. 7, 2022. [Online]. Available: https://www.airport-technology.com/news/glasgow-airport-installs-radar/

[14] Lockheed Martin. *Seeing Through the Blades*. Accessed: Sep. 7, 2022. [Online]. Available: https://www.lockheedmartin.com/en-us/news/features/2016/seeing-through-the-blades.html

[15] D. Mazel, M. Thakur, R. Rivera, M. Lesmerises, and B. Miller, "Integration and testing of infill radars at travis AFB," in *Proc. Integr. Commun. Navigat. Surveill. Conf. (ICNS)*, Sep. 2020, p. 4F1, doi: 10.1109/ICNS50378.2020.9222946.

[16] TERMA. *Wind Farm Radar Mitigation*. Accessed: Sep. 7, 2022. [Online]. Available: https://www.terma.com/markets/ground/wind-farms/radar-mitigation/

[17] (2022). *Airport Surveillance Radar: Scanter 4002*. Accessed: Sep. 7, 2022. [Online]. Available: https://www.terma.com/media/dogb0jqt/termascanter4002_a4_ dec2021.pdf

[18] NATS. *NATS and Raytheon to Deliver Wind Farm Mitigation*. Accessed: Sep. 7, 2022. [Online]. Available: https://www.nats.aero/news/nats-raytheon-deliver-wind-farm-mitigation/

[19] PAGERPOWER. *How It Works—Raytheon Project RM Mitigation*. Accessed: Sep. 7, 2022. [Online]. Available: https://www.pagerpower.com/news/how-it-works-raytheon-project-rm-mitigation/

[20] Thruput. *MIDAS III: Analogue Clutter Mitigation System (ACMS)*. Accessed: Sep. 7, 2022. [Online]. Available: http://www.thruput.co.uk/recording/MIDASIIIACMS

[21] Thruput. *RADIX: Digital Clutter Mitigation System (DCMS)*. Accessed: Sep. 7, 2022. [Online]. Available: http://www.thruput.co.uk/recording/MIDASIVDCMS

[22] Thruput. *Clutter Processing*. Accessed: Sep. 7, 2022. [Online]. Available: http://www.thruput.co.uk/home/product/clutterprocessing.html

[23] AVEILLANT. *Theia 16A: Holographic Radar*. Accessed: Sep. 7, 2022. [Online]. Available: https://www.aveillant.com/wp-content/uploads/2020/02/Theia_16A.pdf

[24] C SPEED. *LightWave Radar*. Accessed: Sep. 7, 2022. [Online]. Available: https://www.cspeed.com/radar

[25] H.-K. Jang, W.-H. Choi, C.-G. Kim, J.-B. Kim, and D.-W. Lim, "Manufacture and characterization of stealth wind turbine blade with periodic pattern surface for reducing radar interference," *Composites B, Eng.*, vol. 56, pp. 178–183, Jan. 2014, doi: 10.1016/j.compositesb.2013.08.043.

[26] TRELLERBORG. *Frame®*. Accessed: Sep. 7, 2022. [Online]. Available: https://www.trelleborg.com/en/applied-technologies/products-and-solutions/radar-mitigation/frame

[27] P. D. Kanhere et al., "Microwave absorbing composite for turbine blade applications," U.S. Patent 103 536 B2, Jul. 16, 2019.

[28] A. Tennant, "Radar-absorbing materials," in *Access Science*, New York, NY, USA: McGraw-Hill Education, 2020, doi: 10.1036/1097-8542.565750.

[29] D. A. Crocker. (Sep. 1, 2020). *Wind Turbine Lightning Mitigation System Radar Cross Section Reduction*. Albuquerque. [Online]. Available: https://www.osti.gov/biblio/1664639/

[30] *Cyrrus Radar Mitigation Technology Overview*. Accessed: Sep. 7, 2022. [Online]. Available: https://www.cyrrus.co.uk/project/cyrrus-radar-mitigation-technology-overview/

[31] J. Pidanic, K. Juryca, and H. Suhaitanto, "The analysis of wind farm impact in primary radar system," in *Proc. Int. Conf. Adv. Comput. Sci. Inf. Syst. (ICACSIS)*, Oct. 2017, pp. 15–20, doi: 10.1109/ICACSIS.2017.8355006.

[32] J. Pidanic, K. Juryca, and H. Suhartanto, "The wind farm simulator of reflected signals in primary radar system," in *Proc. Int. Conf. Adv. Comput. Sci. Inf. Syst. (ICACSIS)*, Oct. 2017, pp. 41–46, doi: 10.1109/ICACSIS.2017.8355010.

[33] S. Gazovova, F. Nebus, and J. Perd'och, "The simulation model for the micro-Doppler analysis," in *Proc. New Trends Signal Process. (NTSP)*, Oct. 2020, pp. 1–6, doi: 10.1109/NTSP49686.2020.9229554.

[34] S. Gazovova, J. Perdoch, and F. Nebus, "Practical limits for micro-Doppler simulation models in digital signal processing," in *Proc. Commun. Inf. Technol. (KIT)*, Oct. 2021, pp. 1–6, doi: 10.1109/KIT52904.2021.9583747.

[35] PNSN Pacific Northwest Seismic Network. *What is a Spectrogram?*. Accessed: Sep. 7, 2022. [Online]. Available: https://pnsn.org/spectrograms/what-is-a-spectrogram

[36] Vibration Research. *What is a Spectrogram?*. Accessed: Sep. 7, 2022. [Online]. Available: https://vibrationresearch.com/blog/what-is-a-spectrogram/

[37] S. S. Haykin, *Adaptive Filter Theory*, 4th ed. Upper Saddle River, NJ, USA: Prentice-Hall, 2002.

[38] P. S. R. Diniz, *Adaptive Filtering: Algorithms and Practical Implementation*, 4th ed. New York, NY, USA: Springer, 2013.

[39] F. Scholkmann, J. Boss, and M. Wolf, "An efficient algorithm for automatic peak detection in noisy periodic and quasi-periodic signals," *Algorithms*, vol. 5, no. 4, pp. 588–603, 2012, doi: 10.3390/a5040588.

[40] F. Albu, L. T. T. Tran, and S. Nordholm, "The hybrid simplified Kalman filter for adaptive feedback cancellation," in *Proc. Int. Conf. Commun. (COMM)*, Jun. 2018, pp. 45–50, doi: 10.1109/ICComm.2018.8430141.

[41] R. E. Kalman, "A new approach to linear filtering and prediction problems," *Trans. ASME, D, J. Basic Eng.*, vol. 82, pp. 35–45, Oct. 1960, doi: 10.1115/1.3662552.

[42] S. J. Julier and J. K. Uhlmann, "Unscented filtering and nonlinear estimation," *Proc. IEEE*, vol. 92, no. 3, pp. 401–422, Mar. 2004, doi: 10.1109/JPROC.2003.823141.

[43] F. Orderud, "Comparison of Kalman filter estimation approaches for state space models with nonlinear measurements," in *Proc. Scand. Conf. Simul. Model.*, 2005, pp. 1–8.

[44] C. Montella. The Kalman Filter and Related Algorithms: A Literature Review. ResearchGate. Accessed: Sep. 7, 2022. [Online]. Available: https://www.researchgate.net/publication/236897001_The_Kalman_Filter_and_Related_Algorithms_A_Literature_Review

[45] J. Shen, Y. Liu, S. Wang, and Z. Sun, "Evaluation of unscented Kalman filter and extended Kalman filter for radar tracking data filtering," in *Proc. Eur. Model. Symp.*, Oct. 2014, pp. 190–194, doi: 10.1109/EMS.2014.49.

[46] K. Juryca, J. Pidanic, and H. Suhartanto, "Prediction of wind turbine's Doppler frequency shifts," in *Proc. New Trends Signal Process. (NTSP)*, Oct. 2020, pp. 1–5, doi: 10.1109/NTSP49686.2020.9229547.

[47] Vestas. *V90-2.0 MW*. Accessed: Sep. 7, 2022. [Online]. Available: https://www.vestas.com/en/products/2-mw-platform/V90-2-0-MW

[48] Wind Turbine Models. *REpower MD77*. Accessed: Sep. 7, 2022. [Online]. Available: https://en.wind-turbine-models.com/turbines/549-repower-md77

[49] Vestas. *V150-4.2 MW*. Accessed: Sep. 7, 2022. [Online]. Available: https://www.vestas.com/en/products/4-mw-platform/V150-4-2-MW

[50] E. A. Wan and R. Van Der Merwe, "The unscented Kalman filter for nonlinear estimation," in *Proc. IEEE Adapt. Syst. for Signal Process., Commun., Control Symp.*, Oct. 2000, pp. 153–158, doi: 10.1109/ASSPCC.2000.882463.

[51] A. Onat, "A novel and computationally efficient joint unscented Kalman filtering scheme for parameter estimation of a class of nonlinear systems," *IEEE Access*, vol. 7, pp. 31634–31655, 2019, doi: 10.1109/ACCESS.2019.2902368.

[52] National Instruments. *USRP-2954 Specifications*. Accessed: Sep. 7, 2022. [Online]. Available: https://www.ni.com/docs/en-US/bundle/usrp-2954-specs/page/specs.html#
[53] *Jirous Antennas*. Accessed: Sep. 7, 2022. [Online]. Available: https://en.jirous.com/
[54] Mini Circuits. *ZHL-16W-43-S+*. Accessed: Sep. 7, 2022. [Online]. Available: https://www.minicircuits.com/WebStore/dashboard.html?model=ZHL-16W-43-S%2B
[55] *GNU Radio*. Accessed: Sep. 7, 2022. [Online]. Available: https://www.gnuradio.org/
[56] *MATLAB—MathWorks–MATLAB & Simulink*. Accessed: Sep. 7, 2022. [Online]. Available: https://www.mathworks.com/products/matlab.html

KAREL JURYCA (Member, IEEE) received the M.Sc. degree from the University of Pardubice, in 2016, where he is currently pursuing the Ph.D. degree. Since 2019, he has been working as an Assistant with the Faculty of Electrical Engineering and Informatics, University of Pardubice. His research interests include radar systems, radar signal processing, and tracking algorithms.

JAN PIDANIC (Senior Member, IEEE) was born in 1979. He received the M.Sc. and Ph.D. degrees from the University of Pardubice, in 2005 and 2012, respectively. His research interests include signal processing in passive radar systems, bistatic radars, clutter modeling, and optimization of signal processing algorithms with parallel processing techniques.

AMIT K. MISHRA (Senior Member, IEEE) received the Ph.D. degree from the University of Edinburgh. He worked in Australia and India. He is currently a Professor with the Department of Electrical Engineering, University of Cape Town (ranked at 157 by THE in 2021). He has successfully supervised nine Ph.D. students so far and holds five patents. Currently, he is the Head of the Centre for 5G in SDG which works on projects related to the application of 5G in challenges related to sustainable development goals. His research interests include radar system design and applied machine learning.

ZLATAN MORIC received the M.S. degree in computer science from the Algebra University College, Zagreb, Croatia, in 2015. He is currently pursuing the Ph.D. degree in information technologies with the Faculty of Information Studies, Novo Mesto, Slovenia. He was the Head of the Cyber Security Department, Algebra University College, where he is a Senior Lecturer.

PAVEL SEDIVY (Senior Member, IEEE) received the M.Sc. degree from the Czech Technical University, Prague, in 1999. He is currently pursuing the Ph.D. degree with the University of Pardubice. He is the Principal Systems Engineer and the Head of the Technical Support Department, RETIA, a.s. His research interests include systems engineering, radar system design, and radar signal processing.